Journal of
Applied Physics

RESEARCH ARTICLE | NOVEMBER 22 2024

Oxygen incorporation effects on the structural and thermoelectric properties of copper(I) iodide

Martin Markwitz ✉ ; Niall Malone ; Song Yi Back ; Alexander Gobbi ; Jake Hardy ;
Peter P. Murmu ; Takao Mori ; Ben J. Ruck ; John V. Kennedy

J. Appl. Phys. 136, 205702 (2024)
https://doi.org/10.1063/5.0235467

AIP Publishing

Journal of
Applied Physics

ARTICLE

pubs.aip.org/aip/jap

Oxygen incorporation effects on the structural and thermoelectric properties of copper(I) iodide

Cite as: J. Appl. Phys. **136**, 205702 (2024); doi: 10.1063/5.0235467
Submitted: 27 August 2024 · Accepted: 3 November 2024 ·
Published Online: 22 November 2024

Martin Markwitz,[1,2,3,a)] Niall Malone,[2,3] Song Yi Back,[4] Alexander Gobbi,[2] Jake Hardy,[1,2,3]
Peter P. Murmu,[2] Takao Mori,[4,5] Ben J. Ruck,[1,3] and John V. Kennedy[2,3]

AFFILIATIONS

[1]School of Chemical and Physical Sciences, Victoria University of Wellington, PO Box 600, Wellington 6140, New Zealand
[2]National Isotope Centre, GNS Science, PO Box 30368, Lower Hutt 5010, New Zealand
[3]The MacDiarmid Institute for Advanced Materials and Nanotechnology, Victoria University of Wellington, PO Box 600, Wellington 6140, New Zealand
[4]International Center for Materials Nanoarchitectonics (WPI-MANA), National Institute for Materials Science (NIMS), 1-1 Namiki, Tsukuba, Ibaraki 305-0044, Japan
[5]Graduate School of Pure and Applied Science, University of Tsukuba, 1-1-1 Tennodai, Tsukuba, Ibaraki 305-8671, Japan

[a)]**Author to whom correspondence should be addressed:** martin.markwitz@vuw.ac.nz

ABSTRACT

Oxygen is a ubiquitous contaminant in thin films grown in high vacuum systems, and it was hypothesized to play an important role in the properties of the *p*-type conductivity of transparent copper(I) iodide, CuI. We study the ambient properties of CuI deposited at various partial pressures of oxygen gas. Through a variety of experimental techniques, we find that achieving a critical oxygen partial pressure of below $p(O_2) = 3 \times 10^{-5}$ mbar is essential for depositing stoichiometric and conductive CuI thin films. Notably, we relate the commonly reported copper excess to the presence of oxygen within the CuI films. Notably, we relate the commonly reported excess of copper in CuI thin films to to the presence of oxygen. Finally, we infer from transport and optical measurements that the hole transporting properties of sputtered CuI films are dominated by an abundance of V_{Cu} defects with an acceptor transition energy of 84 ± 3 meV rather than O_I defects with an acceptor transition energy of 175 ± 14 meV.

I. INTRODUCTION

Transparent conducting materials offer the potential for the development of invisible electronics for everyday use. Currently, inorganic *n*-type transparent conducting oxides dominate such a commercial market with the leading In_2O_3:Sn possessing an optical gap greater than 3 eV and an electrical conductivity near $\sigma \approx 10^4\,\mathrm{S\,cm^{-1}}$, both of which are crucial parameters.[1,2] On the other hand, inorganic *p*-type transparent conductors are limited to the order of $\sigma \approx 10^2\,\mathrm{S\,cm^{-1}}$. Of those compounds, CuI possesses the highest conductivity and optical transparency, derived from a large bandgap of $E_G = 3.1$ eV, high thin film carrier mobility of up to $\mu \approx 20\,\mathrm{cm^2\,V^{-1}\,s^{-1}}$, and high dopability with copper vacancies.[3] The high electrical performance of the ambient room temperature zincblende phase γ-CuI is derived from the diffuse hybridized Cu 3*d* and I 5*p* valence band, with two degenerated bands with low ($m_l = 0.3m_0$), and high ($m_h = 2.4m_0$) effective mass hole bands where m_0 is the free electron mass.[4,5]

CuI leads its competitor *p*-type transparent conductors due to the localization of the O 2*p* valence band in delafossites and strong polaron scattering of the carriers, leading to significantly lower carrier mobilities in such materials.[1,6,7] CuI is *p*-type doped with copper vacancies (V_{Cu}) acting as shallow acceptor states with a thermodynamic activation energy between 78 and 150 meV.[8–10] The unintentional doping with V_{Cu} can push CuI to the point of degenerate conductivity with carrier concentrations beyond $10^{20}\,\mathrm{cm^{-3}}$ while simultaneously maintaining its high mobility.[11–13] Due to the dual-band nature with a heavy carrier band, CuI possesses a large Seebeck coefficient ($\alpha \approx 200\,\mu\mathrm{V\,K^{-1}}$),[14,15] imbuing it with a thermoelectric figure of merit of $ZT = 0.21$.[16–18] High thermoelectric power conversion efficiencies rely on a large thermoelectric figure of merit ($ZT = \alpha^2\sigma T/\kappa$), wherein $\kappa = \kappa_e + \kappa_p$ is the thermal conductivity separated by the carrier and phonon contributions and T is the temperature. Notably, CuI has a low lattice thermal conductivity of $\kappa_p \approx 0.5\,\mathrm{W\,m^{-1}\,K^{-1}}$ due to the large mass of I.[16] Its earth-abundant and non-toxic constituents with facile thin film and powder synthesis methods makes CuI an attractive candidate for potential low-cost device integration for thermoelectric and other applications.[19]

The comparatively limited conductivity of CuI is partially due to its only recent rediscovery as a high performance optoelectronic material.[4,6] Theoretical research found that the lighter chalcogenides O, S, and Se could be promising *p*-type dopants when substituted onto the iodine site.[11] The computationally predicted most promising extrinsic dopant was S due to its shallow thermodynamic transition energy, ranging from 0.215 to 0.33 eV.[11–13] The other chalcogens (O, Se, and Te) have low solubility limits due to the greater formation energy of the introduced acceptor state, and their incorporation is inhibited by the formation of secondary Cu-chalcogen phases. Experimentally, there have been a plethora of recent advancements in the carrier concentration (and thereby conductivity) of CuI in recent years by (a) enhancing the intrinsic properties of CuI by deposition and exposure to I-rich conditions,[6,20] (b) extrinsic shallow acceptor introduction with S or Se doping,[7,21–23] and (c) extrinsic doping to enhance the intrinsic properties with Cs, Al, Fe, or Tb.[24–28] These improvements have brought CuI closer to the $10^3\,\mathrm{S\,cm^{-1}}$ threshold for potential commercial transparent conductor applications, such as in thin film transistors,[29] thermoelectric generators,[18] perovskite-based solar cells,[30] and diodes.[31] The high electrical conductivity and transparency of *p*-type CuI is also important for high power conversion efficiency in an inverted perovskite solar cell architecture.[32,33]

Similarly to S and Se, O has also been clearly identified as a *p*-type dopant in CuI,[34–37] but its role in the measured electrical properties is not yet clear. Challenging the conventional view that it is the copper vacancies, which promote high film carrier concentrations, research by Storm *et al.*[34] suggests that oxygen acceptor defects are the reason for high conductivity in CuI. In addition, it is also understood that CuI undergoes a transient electrical transport property changes through atmospheric exposure.[34,38] To achieve high conductivity and transparency, sputtering or pulsed laser deposition is known to be useful to prepare CuI with high carrier mobility ($>10\,\mathrm{cm^2\,V^{-1}\,s^{-1}}$) and low roughness (<5 nm).[6,7] However, in such vacuum deposition processes, there is a poor understanding of how residual O_2 within the chamber during CuI film deposition (potentially provided by an impure carrier gas) contributes to the measured properties of the material compared to Cu_2O or In_2O_3:Sn.[39,40]

Focusing on the thermoelectric application where CuI is the leading *p*-type candidate, there is to our best knowledge no systematic report for the role of O doping on the thermoelectric properties of CuI. In this paper, we prepared CuI films through reactive ion beam sputtering with various partial O_2 gas pressures. We conducted optical, compositional, structural, and transport measurements to characterize the effect of the oxygen partial pressure [p(O_2)] on the properties of the films, finding a notable change once p(O_2) during deposition was raised to near 1×10^{-4} mbar. We identified the cause for the common [Cu]/[I] excess measured in composition measurements to be due to O incorporation.

II. METHODS

The Si(001), 500 nm thermally oxidized Si(001), microscope slides, and vitreous carbon substrates were cleaned by sonication in acetone, ethanol, and de-ionized water for 10 min each prior to CuI deposition. The reactive ion beam sputtering was conducted under high vacuum. The base pressure of the sputter system was $\leq 3 \times 10^{-7}$ mbar during continuous pumping with a turbopump.[41] A liquid nitrogen cold trap was used to further reduce the residual gas pressure prior to sputtering. For sputtering, Ar gas was fed into the Penning ion source region, some of which entered the deposition chamber region while the gate valve separating the two regions was open. This results in a necessary operating argon partial pressure of p(Ar) = 8×10^{-6} mbar in the deposition chamber region. For controlled oxygen incorporation, 99.99 % O_2 gas was leaked directly into the deposition chamber through a needle valve with a closed gate valve between the Penning ion source and deposition chamber regions, providing a measurement and control of p(O_2). Then, the gate valve separating the Penning ion source and deposition chamber was opened, and sputtering was started. Since the Penning ion source region volume was much lower than that of the deposition chamber the p(O_2) variation before and after opening the gate valve was negligible. The chamber pressure was kept constant during deposition by constantly flooding the chamber with oxygen to replenish the oxygen gas extracted through the turbopumps. This continuous oxygen input provided precise p(O_2) control between 3×10^{-6} and 1×10^{-4} mbar. Sputtering was conducted with an Ar^+ ion beam impinging on a commercial CuI sputter target held at 45°, and substrate holders held at 60° relative to the baseplate. An accelerating voltage of 16 kV with a sputter target current of 0.15 mA was used to deposit the CuI thin films on the aforementioned substrates. The film deposition rate depended on the deposition pressure but was ranged between 0.5 and $1\,\mathrm{nm\,min^{-1}}$.

Rutherford backscattering spectrometry (RBS) measurements were conducted with a 2.0 MeV $^4He^+$ beam with a beam current below 10 nA by using a surface barrier detector mounted at a backscattering angle of 165°.[42] A 100 nm thin film of Gold deposited on a Si(001) substrate and Si(001) with a 500 nm oxidized layer were used for the energy calibration. To investigate the crystallinity of the films, angle-symmetric x-ray diffraction (XRD) was conducted in the $\theta/2\theta$ geometry with a Rigaku SmartLabs diffractometer using a copper x-ray source with a principal x-ray wavelength of $\lambda = 1.54059$ Å. A Ni filter was used to remove Cu K β and W L α-derived diffraction peaks from the diffraction patterns. Transmittance spectrometry was conducted by using a Perkin Elmer Lambda 365 spectrophotometer over a wavelength range between 300 and 800 nm. Steady-state photoluminescence (PL) measurements were performed using a 375 nm Thorlabs L375P70MLD 70 mW light source with a Kymera 328i Spectrograph. Room temperature Hall effect and four-terminal resistance measurements were conducted with a 10 μA driving current by using the HMS-3000 Hall effect measurement system. A 0.55 T permanent magnet was used for the Hall effect measurements. Gold contacts with approximate thicknesses of 100 nm were deposited by ion beam sputtering

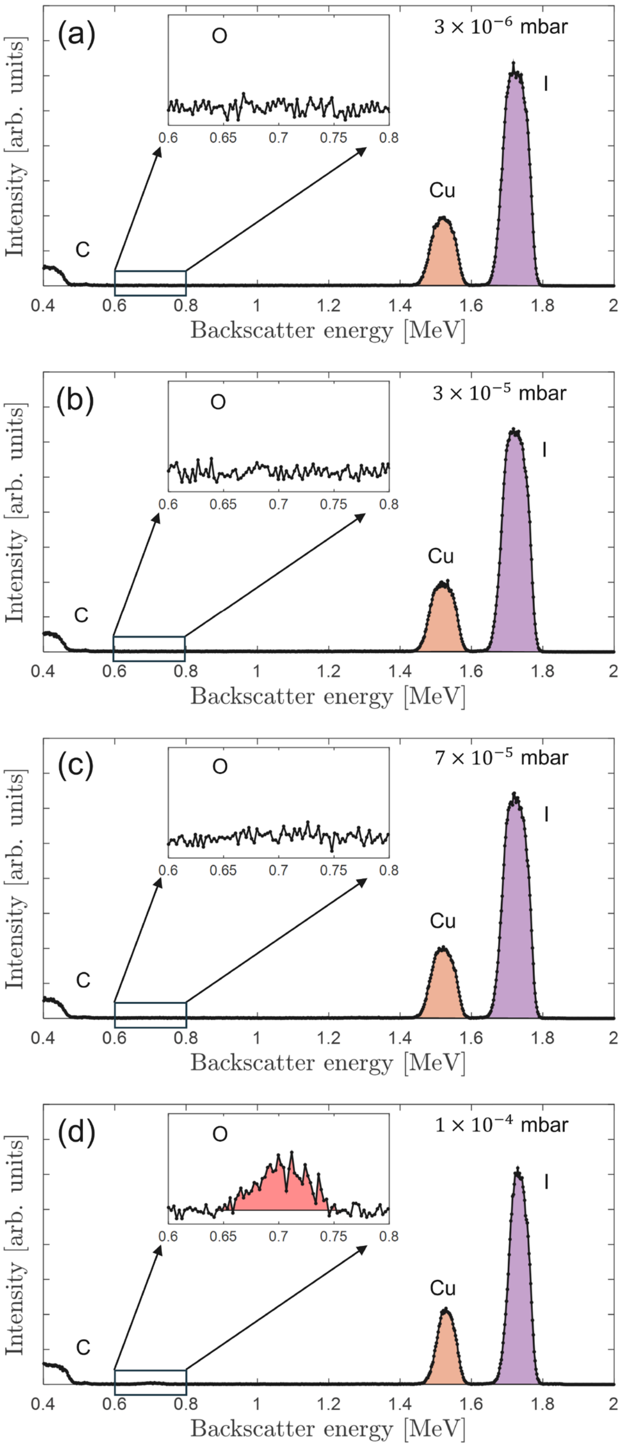

FIG. 1. Rutherford backscattering spectra of films deposited on vitreous carbon at partial pressures of (a) 3×10^{-6}, (b) 3×10^{-5}, (c) 7×10^{-5}, and (d) 1×10^{-4} mbar. The inset graphs show the absence or presence of oxygen in the respective films.

on the corners of the CuI samples through a mask. The Hall effect conductivity and Hall coefficient uncertainties are 5 % of the measured values. Near-room temperature Seebeck effect measurements were conducted in an ULVAC ZEM-3 Seebeck effect measurement system. The Seebeck coefficient uncertainty is 6 % of the measured value.

III. RESULTS AND DISCUSSION

RBS measurements on vitreous carbon substrates were conducted to investigate the degree of oxygen incorporation when CuI is deposited at a variety of oxygen partial pressures (Fig. 1). From the measured data the film compositions were derived from the peak areas and their respective Rutherford scattering cross sections,[43] the results of which are summarized in Table I. The films deposited at and below $p(O_2) = 7 \times 10^{-5}$ mbar showed no presence of oxygen and a near-unitary ratio of [Cu]/[I] [Figs. 1(a)–1(c)] while the film deposited at $p(O_2) = 1 \times 10^{-4}$ mbar [Fig. 1(d)] revealed a [Cu]/[I] concentration ratio of 1.14 ± 0.01, and an oxygen concentration of 9.0 ± 2.2 %, suggesting a relationship between the incorporated concentration of O and an increase in the [Cu]/[I] fraction.

The RBS data of CuI films deposited on Si substrates are shown in Fig. 2(a). Notably, due to the Si, the in-film O backscattering peak is obfuscated for all films. Figure 2(b) shows the [Cu]/[I] ratios for films deposited on Si and C substrates depending on the $p(O_2)$. This suggests that there is a threshold pressure between $p(O_2) = 7 \times 10^{-5}$ and $p(O_2) = 1 \times 10^{-4}$ mbar above which the deposition leads to the incorporation of O in the CuI films. This incorporated oxygen in the films will likely substitute iodine in CuI or lead to the formation of a secondary oxide phase, both of which are compatible with an increase in the [Cu]/[I] ratio.

XRD measurements were then conducted after the RBS measurements to further investigate the O incorporation effects on the crystallinity and microstrain of the deposited films. The XRD patterns of CuI samples deposited on Si(001) substrates are depicted in Fig. 3(a) for the angle-symmetric $\theta/2\theta$ measurements. The diffractograms show the presence of strongly textured CuI in the $\langle 111 \rangle$ orientation.[14] The CuI(111), CuI(222), and CuI(333) peaks were independently used to derive the out-of-plane lattice constant ($a_\perp$) with Bragg's law $\lambda = 2d_{hk\ell} \sin\theta$, wherein $d_{hk\ell} = a_\perp/\sqrt{h^2 + k^2 + \ell^2}$. The derived out-of-plane lattice constant varied slightly based on the diffraction peak order, suggesting imperfect sample alignment within the goniometer. This alignment error was corrected by use of the

TABLE I. Copper, iodine, and oxygen concentrations and the copper to iodine ratio of CuI films derived from RBS measurements deposited on vitreous carbon substrates deposited at various oxygen partial pressures.

$p(O_2)$ (mbar)	Cu (at. %)	I (at. %)	O (at. %)	[Cu]/[I]
3×10^{-6}	49.7 ± 0.4	49.2 ± 0.2	1.1 ± 2.0	1.01 ± 0.01
3×10^{-5}	49.7 ± 0.4	49.5 ± 0.2	0.7 ± 1.9	1.00 ± 0.01
7×10^{-5}	49.8 ± 0.4	49.1 ± 0.2	1.1 ± 2.2	1.01 ± 0.01
1×10^{-4}	48.5 ± 0.4	42.5 ± 0.2	9.0 ± 2.2	1.14 ± 0.01

goniometer error function $G(\theta) = \frac{1}{2}\cot^2(\theta)[1 + \sin(\theta)]$[3] to derive the true out-of-plane lattice constants, the p(O_2)-dependence thereof depicted in Fig. 3(b). As the partial oxygen pressure increased, the out-of-plane CuI lattice constant monotonically reduced from 6.068 ± 0.001 Å for the films deposited at $p(O_2) \leq 3 \times 10^{-7}$ mbar to 6.055 ± 0.001 Å for the films deposited at $p(O_2) = 1 \times 10^{-4}$ mbar. It is known that room temperature vacuum-deposited CuI films possess larger out-of-plane lattice constants than the bulk powder value of 6.054 Å, with in-plane values that are smaller suggesting that the films are subjected to biaxial tensile strain.[3,4,44] The reducing out-of-plane lattice constant suggests some strain relaxation effects due to a differing chemical composition of the film.

In order to deconvolute macrostrain, microstrain, and broadening effects of the out-of-plane peak series, the Williamson–Hall plot approach was employed. The Williamson–Hall plot approach draws a linear fit $\beta\cos(\theta) = 4\varepsilon\sin(\theta) + K\lambda/D$ through the peak positions and peak widths wherein β is the width (in radians), ε is the strain, K is a numerical constant, and D is the crystallite size.[45] This method was conducted after subtracting a constant systematic broadening approximated by the broadening of the Si(004) substrate peak width.[46] Based on this approach, the out-of-plane crystallite sizes did not significantly vary as the oxygen partial pressure varied. On the other hand, the out-of-plane strain ($\varepsilon_\perp$) at first decreases from $0.94 \times 10^{-3} \pm 0.17 \times 10^{-3}$ for the film deposited at $p(O_2) \leq 3 \times 10^{-7}$ mbar to $0.72 \times 10^{-3} \pm 0.07 \times 10^{-3}$ for the film deposited at $p(O_2) = 3 \times 10^{-5}$ mbar. Subsequently $\varepsilon_\perp$ increased to $1.33 \times 10^{-3} \pm 0.09 \times 10^{-3}$ for the film deposited at $p(O_2) = 1 \times 10^{-4}$ mbar. The derived out-of-plane microstrain relationship with p(O_2) is shown in Fig. 3(c). The $\varepsilon_\perp$ becomes relaxed as the growth pressure increases toward $p(O_2) = 3 \times 10^{-5}$ mbar, while above it, $\varepsilon_\perp$ sharply increases again. The cause for this onset of strain is not yet understood, but due to the low calculated solubility of chalcogenides in CuI,[8,12,14,21] it is possible that a secondary oxide phase becomes incorporated in the films.[36,37] In summary, it is reasonable to interpret that the variation of the structural properties are related to variations in the chemical composition of the films, which itself can be controlled by variation of the p(O_2) during deposition.

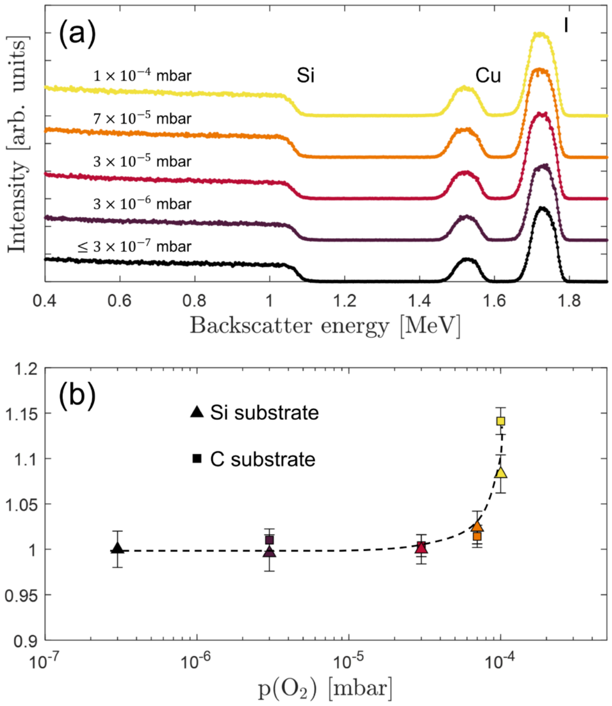

FIG. 2. (a) Rutherford backscattering spectra of films deposited on silicon at a variety of oxygen partial pressures [p(O_2)]. (b) Copper-to-iodine ratio depending on p(O_2). The dashed line is used to guide the reader.

To investigate variations in the transport properties of the samples, they were subjected to four-point van der Pauw electrical conductivity measurements, the results of which are summarized in Table II. The films deposited at $p(O_2) \leq 3 \times 10^{-7}$ mbar exhibited an electrical conductivity of 65.7 ± 2.4 S cm^{-1}, which did not change significantly over a wide range of oxygen partial pressures. Notably, the films deposited at $p(O_2) = 1 \times 10^{-4}$ mbar had a reduced electrical conductivity of 39.9 ± 1.8 S cm^{-1}. The samples were subjected to room temperature Hall and Seebeck effect measurements, which identified *p*-type carrier conduction in all films. The carrier concentration was derived from the Hall coefficient through $p_H = (qR_H)^{-1}$, and the carrier mobility was derived from $\mu = \sigma R_H$. The Hall factor was assumed to be unitary due to the high carrier concentrations in these films. Hall carrier mobilities of 8.7 ± 0.8 $\text{cm}^2\,\text{V}^{-1}\,\text{s}^{-1}$ were found for the samples deposited at $p(O_2) \leq 3 \times 10^{-7}$ mbar, which increased to 9.4 ± 0.8 $\text{cm}^2\,\text{V}^{-1}\,\text{s}^{-1}$ for the samples deposited at $p(O_2) = 7 \times 10^{-5}$ mbar, and reduced to 6.5 ± 1.8 $\text{cm}^2\,\text{V}^{-1}\,\text{s}^{-1}$ for the samples deposited at $p(O_2) = 1 \times 10^{-4}$ mbar. The Hall carrier concentration derived from the Hall coefficient remained approximately constant near 4.2×10^{19} cm^{-3} for all films (comparable to previously measured values[14,15]). The series of films produced similar Seebeck coefficients (≈200 μV K^{-1}), except for the film deposited at $p(O_2) \leq 3 \times 10^{-7}$ mbar, which provided a greater Seebeck coefficient of 235 ± 14 μV K^{-1}.

The increased mobility at moderate oxygen partial gas pressures is similar to the results by Storm *et al.*,[3] who instead used nitrogen as a background gas during deposition of CuI with pulsed laser deposition. Depositing CuI at moderate gas pressures results in an improved crystal quality, in this case identified by a reduction in the microstrain, therefore improving the carrier mobility by a reduction of the concentration of scattering sites. The cause for the reduced carrier mobility for the film deposited at the highest oxygen partial pressure was presumably due to scattering from the increased concentration of additional oxygen defects and oxide impurities. Finally, the power factor ($\alpha^2\sigma$) derived for the films is greatest for those deposited at $p(O_2) \leq 3 \times 10^{-7}$ mbar, finding a power factor of 363 ± 45 μW $\text{m}^{-1}\,\text{K}^{-2}$, reducing to 168 ± 22 μW $\text{m}^{-1}\,\text{K}^{-2}$ for the films deposited at $p(O_2) = 1 \times 10^{-4}$ mbar. This implies that for thermoelectric applications CuI should be deposited at the lowest possible p(O_2), while it does not strongly affect the electrical properties. Overall, oxygen does not appear to have a strong effect on the carrier concentration and Seebeck coefficient, implying that the O_I acceptor energy is deeper within the bandgap than the V_{Cu} acceptor

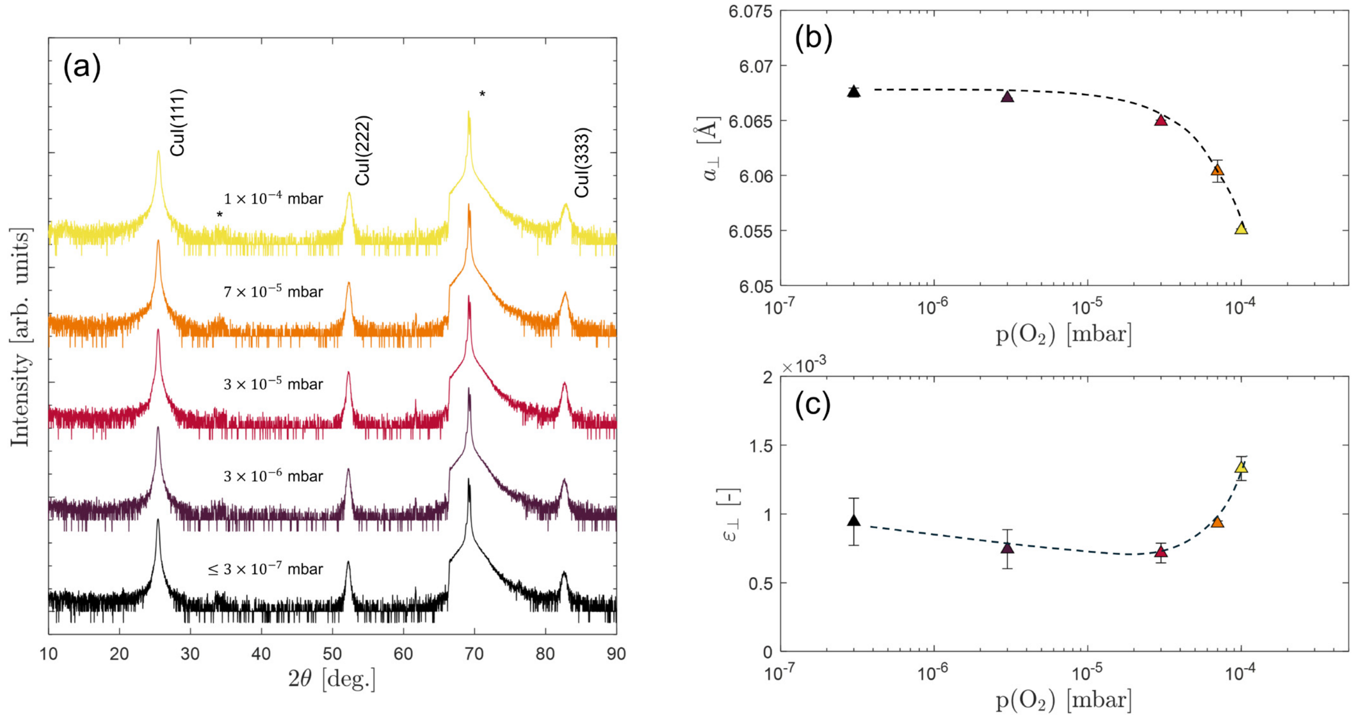

FIG. 3. (a) Labeled $\theta/2\theta$ x-ray diffraction patterns of CuI films deposited on thermally oxidized silicon substrates at various oxygen partial pressures. Calculated (b) out-of-plane lattice constant $a_\perp$ and (c) out-of-plane strain $\varepsilon_\perp$ from the diffraction patterns. The dashed lines are used to guide the reader.

energy, and that there is a low concentration thereof. Further, the low solubility limit of oxygen in CuI limits the concentration of O_I acceptors,[11] which could instead lead to forming oxide phases, which provide a limited contribution to the conductivity in the films.[37]

The samples' optical properties were measured with transmittance spectrometry and PL. The transmittance spectra are depicted in Fig. 4(a), which show that the samples deposited at $p(O_2) \leq 3 \times 10^{-5}$ mbar) have high transmittance (>70%) throughout the highlighted visible regime. These samples also clearly exhibit the characteristic CuI Z_1/Z_2 (3.10 ± 0.01 eV) and the spin orbit split Z_3 (3.73 ± 0.01 eV) excitonic absorption resonances.[3] The Z_1/Z_2 absorption is at ~0.05 eV higher than the standard value of 3.05 eV,[4] possibly due to the high carrier concentrations in these films which would cause a blueshift in the excitonic absorption energy.[25,47] The samples deposited at $p(O_2) > 3 \times 10^{-5}$ mbar exhibit slightly lower average transmittances with values of 65%–67%, and appear to have suppressed excitonic absorption resonances.

The generalized Elliot formula was used in order to investigate the absorption properties (single particle gap energy E_G, spectral broadening Γ, and exciton binding energy $E_{B,i}$) of the deposited films, a method recently finding use for analyzing absorption data of perovskite compounds.[48,49] This type of absorption model considers two types of absorption: excitonic absorption peaks, and the continuum band-to-band transition absorption contribution, which also include band nonparabolicity and Sommerfeld enhancement effects, written as

TABLE II. Room temperature electrical and thermoelectric properties of CuI thin films deposited at different oxygen partial pressures.

$p(O_2)$ (mbar)	σ (S cm^{-1})	μ_H (cm^2 V^{-1}s^{-1})	p_H ($\times 10^{19}$ cm^{-3})	α (μV K^{-1})	$\alpha^2\sigma$ (μW m^{-1} K^{-2})
$\leq 3 \times 10^{-7}$	65.7 ± 2.4	8.7 ± 0.8	4.7 ± 0.3	235 ± 14	363 ± 45
3×10^{-6}	61.3 ± 2.3	9.2 ± 0.8	4.2 ± 0.2	200 ± 12	245 ± 31
3×10^{-5}	57.9 ± 2.1	9.4 ± 0.8	3.9 ± 0.2	198 ± 12	227 ± 28
7×10^{-5}	64.2 ± 2.4	9.3 ± 0.9	4.3 ± 0.3	207 ± 12	275 ± 34
1×10^{-4}	39.9 ± 1.8	6.5 ± 1.8	3.9 ± 0.9	205 ± 12	168 ± 22

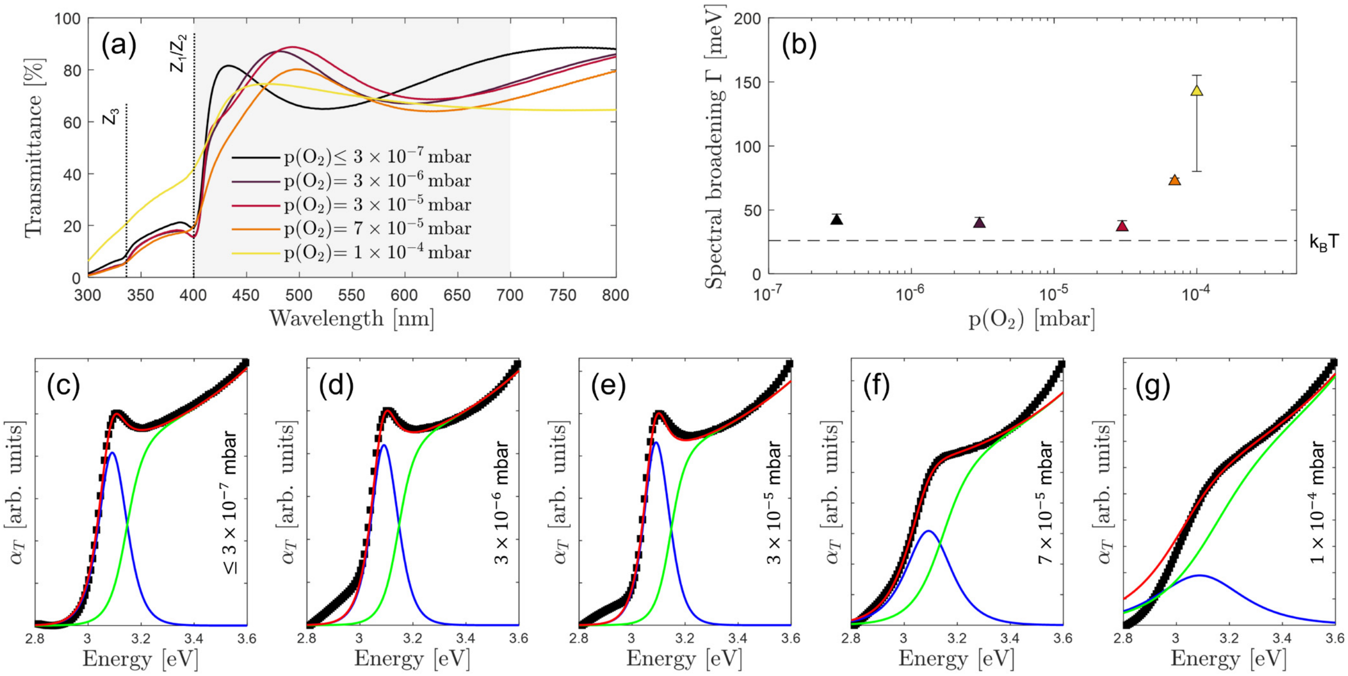

FIG. 4. (a) Transmittance spectra with highlighted visible region and annotated excitonic absorption energies. The room temperature thermal energy k_BT is highlighted with the dashed line. (b) Spectral broadening factor derived from Elliot fits (red) comprised of excitonic (blue) and continuum (green) components, which are shown in (c)–(g).

$$\alpha_T(\hbar\omega) \propto \frac{1}{\hbar\omega}\sum_i\left[\sum_n \frac{2E_{B,i}}{n^3}\,\mathrm{sech}\left(\frac{\hbar\omega - E_{B,n,i}}{\Gamma}\right) + \int_{E_G}^{\infty}\mathrm{sech}\left(\frac{\hbar\omega - E}{\Gamma}\right)\frac{1}{1-\exp\left(-2\pi\sqrt{\frac{E_{B,i}}{E-E_G}}\right)}\frac{1}{1-\frac{8\mu_i^2 b}{\hbar^4}(E-E_G)}\,\mathrm{d}E\right] \tag{1}$$

for a two-valence band system $i = l, h$ considering contribution from both light and heavy holes, n is the exciton order, $E_{B,n,i} = E_G - E_{B,i}n^{-2}$ is the nth order exciton binding energy analogous to the electron energy levels of the hydrogen atom, $\mu_i = m_i m_e(m_i + m_e)^{-1}$ is the reduced mass for each absorption channel, and b is band nonparabolicity defined through $E_{CB}(\vec{k}) - E_{V,i}(\vec{k}) = E_G + \hbar^2\left|\vec{k}\right|^2(2\mu_i)^{-1} - b\left|\vec{k}\right|^4$. To fit Eq. (1) to the measured data, the absorption coefficient (α_T) was derived through $\alpha_T = z^{-1}\ln(1/T')$, where T' is the sample transmittance. The sample reflectance was assumed much less than one ($R' \ll 1$). An electron effective mass $m_e = 0.23m_0$, a single particle bandgap $E_G = 3.145$ eV, and a band nonparabolicity factor $b = 0.55$ eV m^4 were found to provide good absorption profiles that fitted the experimental results. This allowed the spectral broadening Γ to be fitted as the only free variable, a descriptor for instrumental and sample-derived broadening factors. The derived spectral broadening factors Γ are depicted in Fig. 4(b) while the Elliot fits themselves are shown in Figs. 4(c)–4(g). The variation in the broadening factor Γ appears to be coupled to the evolution of the microstrain, suggesting that there is a relationship between the two. The exciton binding energies were calculated with $E_{B,i} = \mu_i q^4\left(2(4\pi\varepsilon)^2\hbar^2\right)^{-1}$ where $\varepsilon = \varepsilon_r\varepsilon_0$ using $\varepsilon_r = 6.5$.[4] The choice of electron effective mass resulted in binding energies of $E_{B,l} = 42$ meV and $E_{B,h} = 68$ meV for the light and heavy hole-derived excitons, respectively. Due to the greater hole effective mass and, therefore, exciton binding energy and absorption intensity, the excitonic absorption derived from the heavy hole band dominates the excitonic absorption data. The derived exciton binding energies are similar to those reported by Nikitine[50] and Inagaki *et al.*[44] of ≈62 meV. The weighted average exciton binding energy is 54 meV, and the lower binding energy is likely a result of the electron effective mass and the higher free carrier concentration as expected by the model of excitons by Mahan.[47] This type of analysis using the Elliot fit is recommended anytime the presence of excitonic states influences the absorption spectra of a compound[49,51] and is used in this work for determining the bandgap of CuI rather than the commonly used Tauc plot fitting procedure. The Tauc plot procedure uses the low-energy shoulder of the excitonic absorption spectrum rather than the basic assumption of absorption due to a parabolic band absorption edge, which categorically underestimates the bandgap of CuI as 3.0 eV compared to the more-realistic value of $E_G = 3.1$ eV.

Steady-state PL spectra were conducted to investigate the evolution of shallow acceptor states in CuI as a function of deposition pressure which are shown in Fig. 5. Three gaussian functions were used to resemble PL emissions derived from excitonic recombination (red), V_{Cu} defects (green), and $\mathrm{O_I}$ defects (blue). Beyond the $p(\mathrm{O_2}) = 3 \times 10^{-5}$ mbar threshold pressure, the PL spectra of the CuI films showed an increased high-wavelength shoulder of the PL data, attributed the incorporation of $\mathrm{O_I}$ defects. Notably, the PL intensity of the $\mathrm{O_I}$ defect relative to the other PL peaks scaled with the deposition pressure. The emission energies (and peak full width at half maxima) were restricted to 2.990 ± 0.001 (0.045 ± 0.001), 2.958 ± 0.002 (0.077 ± 0.003), and 2.869 ± 0.013 eV $(0.114 \pm 0.006$ eV$)$, for the excitonic,[52] V_{Cu},[53] and $\mathrm{O_I}$-derived emission lines, respectively. If the energy difference between the exciton emission energy from PL to the bandgap is assumed to be identical to the (average) exciton binding energy, the V_{Cu} defect states lay 84 ± 3 meV above the valence band maximum, while the $\mathrm{O_I}$ defect states lay 175 ± 14 meV above the valence band maximum. Storm *et al.*,[8] Bar *et al.*,[9] and Koyasu *et al.*[10] derived a V_{Cu} acceptor energy of 78, 95, and 150 meV, with which our results are in good agreement. Also, density functional theory using the Perdew–Burke–Ernzerhof exchange correlation functional with a Hubbard parameter applied to the Cu 3*d* states calculations found that the $\mathrm{O_I^0}$ to $\mathrm{O_I^{1\text{-}}}$ acceptor transition is ≈100 meV deeper than the V_{Cu}^0 to $V_{\mathrm{Cu}}^{1\text{-}}$ acceptor transition.[11] A schematic of the CuI valence band structure and the acceptor energy levels is visualized in Fig. 6. In our films, the limited effectiveness of the $\mathrm{O_I}$ acceptor is further masked by the abundance of V_{Cu} acceptors in the present films, in contrast with the films grown by Storm *et al.*,[34] which possess overall lower carrier concentrations ($\approx 10^{17}$ cm^{-3}).

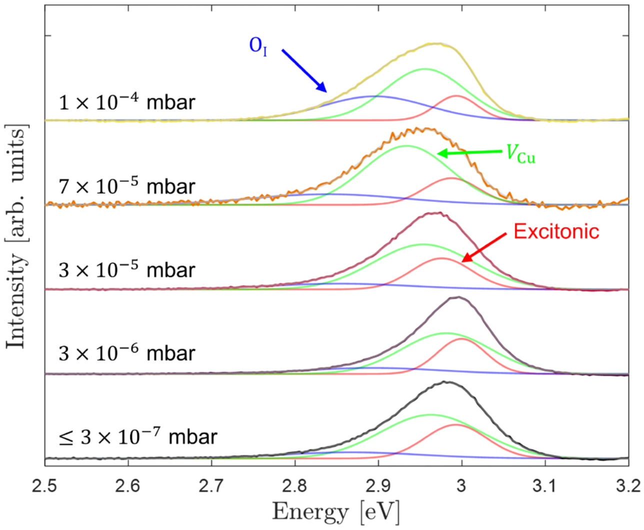

FIG. 5. (a) Normalized PL spectra fitted with gaussian functions resembling excitonic (red), V_{Cu} (green), and $\mathrm{O_I}$ (blue) PL features.

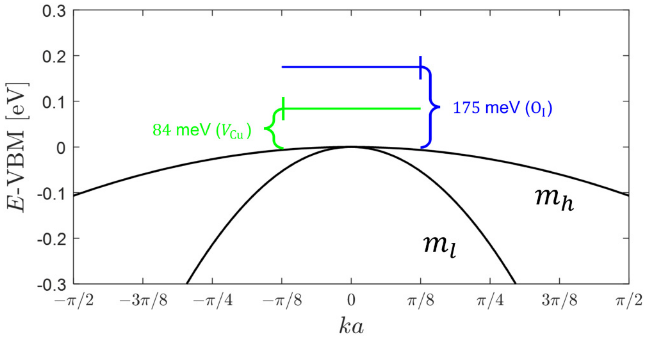

FIG. 6. Near-valence band structure schematic with parabolic light (m_l) and heavy (m_h) bands, and the positions of V_{Cu} and $\mathrm{O_I}$ acceptors relative to the valence band.

IV. CONCLUSION

The aim of this work was to investigate whether small concentrations of O have notable effects on the optical and transport properties of CuI thin films. This research clarifies how the O partial pressure plays a role in the measured electrical and optical properties of CuI films, and finds that the properties of CuI are insensitive to the O partial pressure at or below a threshold pressure of $p(\mathrm{O_2}) = 3 \times 10^{-5}$ mbar. The electrical, optical, and structural properties notably vary above this threshold pressure, where a O is incorporated in the films, as measured with RBS. The highest mobility of the CuI films is observed when deposited at a moderate partial pressure, which suggests a potential direction for achieving heavily doped and high mobility CuI film deposition.

The controlled gas partial pressure environment we used to incorporate O in our films is not compositionally equivalent to air as it is missing other gaseous constituents such as nitrogen. For CuI, however, O is expected to be the active ingredient in air, which can be incorporated during film deposition. This is important information for reducing the time needed to pump down vacuum systems from atmosphere before CuI film deposition and, therefore, reducing the cost of such a process. The V_{Cu} defect is found to be a shallower acceptor in CuI than $\mathrm{O_I}$ by ≈100 meV, suggesting that O is not an effective *p*-type dopant in already heavily doped CuI.

ACKNOWLEDGMENTS

This research was funded by the Royal Society of New Zealand through the Marsden Fund, New Zealand (Grant No.

MFP-GNS2301) and the JST Mirai Program, Japan (Grant No. JPMJMI19A1). The authors wish to acknowledge Mr. Chris Purcell (National Isotope Centre, GNS Science, New Zealand) for carrying out RBS measurements.

AUTHOR DECLARATIONS

Conflict of Interest

The authors have no conflicts to disclose.

Author Contributions

Martin Markwitz: Conceptualization (equal); Data curation (lead); Formal analysis (equal); Investigation (lead); Methodology (equal); Visualization (equal); Writing – original draft (lead); Writing – review & editing (equal). **Niall Malone:** Conceptualization (equal); Formal analysis (equal); Validation (equal); Visualization (equal); Writing – review & editing (equal). **Song Yi Back:** Data curation (equal); Writing – review & editing (equal). **Alexander Gobbi:** Data curation (equal); Investigation (equal); Writing – review & editing (equal). **Jake Hardy:** Data curation (equal); Writing – review & editing (equal). **Peter P. Murmu:** Funding acquisition (equal); Resources (equal); Supervision (equal); Validation (equal); Writing – review & editing (equal). **Takao Mori:** Resources (equal); Supervision (equal); Writing – review & editing (equal). **Ben J. Ruck:** Formal analysis (equal); Funding acquisition (equal); Supervision (equal); Validation (equal); Writing – review & editing (equal). **John V. Kennedy:** Funding acquisition (equal); Project administration (equal); Resources (equal); Supervision (equal); Validation (equal); Writing – review & editing (equal).

DATA AVAILABILITY

The data that support the findings of this study are available from the corresponding author upon reasonable request.

REFERENCES

[1] J. Willis and D. O. Scanlon, J. Mater. Chem. C **9**, 11995 (2021).

[2] M. Markwitz, S. Y. Back, E. X. M. Trewick, P. P. Murmu, T. Mori, B. J. Ruck, and J. V. Kennedy, Phys. Rev. B **109**, 115201 (2024).

[3] P. Storm, M. S. Bar, G. Benndorf, S. Selle, C. Yang, H. von Wenckstern, M. Grundmann, and M. Lorenz, APL Mater. **8**, 091115 (2020).

[4] M. Grundmann, F. L. Schein, M. Lorenz, T. Böntgen, J. Lenzner, and H. von Wenckstern, Physica Status Solidi A **210**, 1671 (2013).

[5] J. Wang, J. Li, and S. S. Li, J. Appl. Phys. **110**, 054907 (2011).

[6] C. Yang, M. Kneiß, M. Lorenz, and M. Grundmann, Proc. Natl. Acad. Sci. U.S.A. **113**, 12929 (2016).

[7] A. S. Mirza, M. Pols, W. Soltanpoor, S. Tao, G. Brocks, and M. Morales-Masis, Matter **6**, 4306 (2023).

[8] P. Storm, M. S. Bar, S. Selle, H. von Wenckstern, M. Grundmann, and M. Lorenz, Physica Status Solidi (RRL) **15**, 2100214 (2021).

[9] M. S. Bar, D. Splith, Y. Chen, M. Grundmann, H. von Wenckstern, T. Rauch, S. Blaurock, and H. Krautscheid, Phys. Rev. Appl. **22**, 044027 (2024).

[10] S. Koyasu, N. Umezawa, J. D. Baniecki, A. Yamaguchi, and M. Miyauchi, Cryst. Growth Des. **18**, 6748 (2018).

[11] D. Huang, Y. J. Zhao, S. Li, C. S. Li, J. J. Nie, X. H. Cai, and C. M. Yao, J. Phys. D: Appl. Phys. **45**, 145102 (2012).

[12] M. Graužinytė, S. Botti, M. A. L. Marques, S. Goedecker, and J. A. Flores-Livas, Phys. Chem. Chem. Phys. **21**(35), 18839–18849 (2019).

[13] J. Willis, R. Claes, Q. Zhou, M. Giantomassi, G. Rignanese, G. Hautier, and D. O. Scanlon, Chem. Mater. **35**, 8995 (2023).

[14] M. Markwitz, P. P. Murmu, S. Y. Back, T. Mori, B. J. Ruck, and J. V. Kennedy, Surf. Interfaces **41**, 103190 (2023).

[15] M. Markwitz, P. P. Murmu, S. Y. Back, T. Mori, J. V. Kennedy, and B. J. Ruck, Mater. Today Phys. **46**, 101513 (2024).

[16] C. Yang, D. Souchay, M. Kneiß, M. Bogner, H. M. Wei, M. Lorenz, O. Oeckler, G. Benstetter, Y. Q. Fu, and M. Grundmann, Nat. Commun. **8**, 16076 (2017).

[17] T. Zhu, Y. Liu, C. Fu, J. P. Heremans, J. G. Snyder, and X. Zhao, Adv. Mater. **29**, 1605884 (2017).

[18] J. Coroa, B. M. Morais Faustino, A. Marques, C. Bianchi, T. Koskinen, T. Juntunen, I. Tittonen, and I. Ferreira, RSC Adv. **9**, 35384 (2019).

[19] A. Liu, H. Zhu, M. G. Kim, J. Kim, and Y. Y. Noh, Adv. Sci. **8**, 2100546 (2021).

[20] E. J. Bae, J. Kim, M. Han, and Y. H. Kang, ACS Mater. Lett. **5**, 2009 (2023).

[21] P. P. Murmu, J. Kennedy, Z. Liu, and T. Mori, J. Alloys Compd. **921**, 166103 (2022).

[22] K. H. Ahn, G. H. Kim, S. J. Kim, J. H. Kim, G. S. Ryu, P. Lee, B. K. Ryu, J. Y. Cho, Y. H. Kim, J. H. Kang *et al.*, Chem. Mater. **34**, 10517 (2022).

[23] P. P. Murmu, M. Markwitz, S. V. Chong, N. Malone, T. Mori, H. Vyas, L. J. Kennedy, S. Rubanov, C. I. Sathish, J. Yi, and J. V. Kennedy, Mater. Today Energy **44**, 101639 (2024).

[24] K. Matsuzaki, N. Tsunoda, Y. Kumagai, Y. Tang, K. Nomura, F. Oba, and H. Hosono, J. Am. Chem. Soc. **144**, 16572 (2022).

[25] A. S. Mirza, B. Vishal, P. Dally, C. S. Schnohr, S. De Wolf, and M. Morales-Masis, Adv. Funct. Mater. **34**, 2316144 (2024).

[26] N. Salah, A. Alshahrie, M. Aljaghtham, A. Saeed, N. Baghdadi, and K. Koumoto, Adv. Electron. Mater. **8**, 2101214 (2022).

[27] S. Byeon, K. Pryga, J. H. Kim, J. S. Rhyee, K. Komedera, B. Wiendlocha, and H. Jin, J. Alloys Compd. **1002**, 175349 (2024).

[28] N. Salah, A. M. Abusorrah, Y. N. Salah, M. Almasoudi, N. Baghdadi, A. Alshahri, and K. Koumoto, Ceram. Int. **46**, 27244 (2020).

[29] A. Liu, H. Zhu, W. T. Park, S. J. Kim, H. Kim, M. G. Kim, and Y. Y. Noh, Nat. Commun. **11**, 4309 (2020).

[30] H. Wang, Z. Yu, X. Jiang, J. Li, B. Cai, X. Yang, and L. Sun, Energy Technol. **5**, 1836 (2017).

[31] C. Yang, M. Kneiß, F. L. Schein, M. Lorenz, and M. Grundmann, Sci. Rep. **6**, 21937 (2016).

[32] S. Z. Haider, H. Anwar, S. Manzoor, A. G. Ismail, and M. Wang, Curr. Appl. Phys. **20**, 1080 (2020).

[33] K. Wang, Z. Xu, Z. Guo, H. Wang, S. M. H. Qaid, K. Yang, and Z. Zang, Adv. Energy Mater. **14**, 2402249 (2024).

[34] P. Storm, S. Gierth, S. Selle, M. S. Bar, H. von Wenckstern, M. Grundmann, and M. Lorenz, APL Mater. **9**, 051101 (2021).

[35] C. S. Herrick and A. D. Tevebaugh, J. Electrochem. Soc. **110**, 119 (1963).

[36] B. L. Zhu and X. Z. Zhao, Physica Status Solidi A **208**, 91 (2011).

[37] R. Xue, G. Gao, L. Yang, L. Xu, Y. Zhang, and J. Zhu, J. Mater. Chem. C **11**, 13681 (2023).

[38] A. Crovetto, H. Hempel, M. Rusu, L. Choubrac, D. Kojda, K. Habicht, and T. Unold, ACS Appl. Mater. Interfaces **12**, 48741 (2020).

[39] S. Shibasaki, Y. Honishi, N. Nakagawa, M. Yamazaki, Y. Mizuno, Y. Nishida, K. Sugimoto, and K. Yamamoto, Appl. Phys. Lett. **119**, 242102 (2021).

[40] P. P. Murmu, A. Shettigar, S. V. Chong, Z. Liu, D. Goodacre, V. Jovic, T. Mori, K. E. Smith, and J. V. Kennedy, J. Materiom. **7**, 612 (2021).

[41] J. Kennedy, P. P. Murmu, J. Leveneur, A. Markwitz, and J. Futter, Appl. Surf. Sci. **367**, 52 (2016).

[42] J. V. Kennedy, A. Markwitz, H. J. Trodahl, B. J. Ruck, S. Durbin, and W. Gao, J. Electron. Mater. **36**, 472 (2007).

[43] J. W. Mayer and E. Rimini, *Ion Beam Handbook for Material Analysis* (Elsevier, 2012).

[44] S. Inagaki, M. Nakamura, Y. Okamura, M. Ogino, Y. Takahashi, L. C. Peng, X. Z. Yu, Y. Tokura, and M. Kawasaki, Appl. Phys. Lett. **118**, 012103 (2021).

[45] G. F. Harrington and J. Santiso, J. Electroceram. **47**, 141 (2021).

[46] A. K. Zak, W. H. A. Majid, M. E. Abrishami, and R. Yousefi, Solid State Sci. **13**(1), 251–256 (2011).
[47] G. D. Mahan, Phys. Rev. **153**, 882 (1967).
[48] F. Ruf, M. F. Aygüler, N. Giesbrecht, B. Rendenbach, A. Magin, P. Docampo, H. Kalt, and M. Hetterich, APL Mater. **7**, 031113 (2019).
[49] T. Palmieri, E. Baldini, A. Steinhoff, A. Akrap, M. Kollár, E. Horváth, L. Forró, F. Jahnke, and M. Chergui, Nat. Commun. **11**, 850 (2020).
[50] S. Nikitine, Philos. Mag. **4**, 1 (1959).
[51] C. Malerba, F. Biccari, C. L. A. Ricardo, M. D'Incau, P. Scardi, and A. Mittiga, Solar Energy Mater. Solar Cells **95**, 2848 (2011).
[52] K. X. Zhang, S. W. Wang, L. Y. Bai, Y. Wang, K. Ou, Y. W. Zhang, and L. X. Yi, J. Lumin. **214**, 116522 (2019).
[53] S. Koyasu, N. Umezawa, A. Yamaguchi, and M. Miyauchi, J. Appl. Phys. **125**, 115101 (2019).